

Tsunami forcing by a low Froude number landslide

Colin Whittaker¹ · Roger Nokes² · Mark Davidson²

Received: 29 July 2014 / Accepted: 18 April 2015 / Published online: 7 May 2015
© Springer Science+Business Media Dordrecht 2015

Abstract The waves generated by a submarine landslide, of great concern to coastal communities, exhibit strong dependence on the landslide motion along the sea floor. A series of two-dimensional physical experiments investigate the waves generated by a solid block landslide moving along a horizontal boundary, allowing measurement of both onshore- and offshore-propagating waves using the laser-induced fluorescence technique. This technique provides high-quality free surface measurements over the entire length of the experimental flume, and hence a data set that can be used to validate numerical models for this idealised scenario. The landslide motion is provided by a mechanical system, allowing testing of a range of landslide accelerations and terminal velocities. The landslide Froude number governs the overall behaviour of the wave field. At lower Froude numbers, the waves are almost entirely generated by the landslide acceleration and deceleration, and the offshore- and onshore-propagating wave groups contain approximately equal energy. Interactions between the landslide and the offshore-propagating waves become more important as the Froude number increases. Two inviscid-irrotational models demonstrate the importance of dispersive effects for tsunamis generated by a submarine landslide, and correctly predict the behaviour of the entire wave field at low Froude numbers. The predictions in the vicinity of the landslide worsen with increasing Froude number, due to the linear free surface conditions used by the models. Lower Froude numbers appear to be more representative of previous sloping-boundary experimental geometries, although rigid block landslides still represent an idealisation of a field scenario.

Keywords Tsunami · Landslide · Laser-induced fluorescence (LIF) · Particle tracking velocimetry (PTV) · Inviscid-irrotational flow

✉ Colin Whittaker
colin.whittaker@plymouth.ac.uk

¹ School of Marine Science and Engineering, Plymouth University, Plymouth PL48AA, UK

² Department of Civil and Natural Resources Engineering, University of Canterbury, Private Bag 4800, Christchurch 8140, New Zealand

1 Introduction

1.1 Landslides as a tsunami source mechanism

Landslide-generated tsunamis pose a threat to people and infrastructure located near to the coast; such waves may also occur in alpine lakes or dam reservoirs. Waves generated by a landslide have large amplitudes in the near field, or in the vicinity of the landslide, and can propagate rapidly to inundate nearby sections of the coast. The proximity of the landslide to the shore allows virtually no time for warning or evacuation of coastal communities. However, the rapid dispersion of landslide-generated waves during their propagation reduces their capacity for transoceanic devastation (in contrast to tsunamis generated by an underwater fault rupture). A combined source mechanism may occur if a landslide is triggered by offshore seismic activity. These waves are likely to become more important in the future as coastal development intensifies, particularly in light of climate-induced sea level rise.

A tsunamigenic landslide may be initiated above or below the water surface; such landslides are defined as subaerial and submarine, respectively. Due to the shallower failure slope and the presence of water as a retarding fluid, a submarine landslide will not move as rapidly as a subaerial landslide [11]. However, submarine landslides are capable of mobilising larger sediment volumes and running out over longer distances than subaerial landslides [21]. The current study focuses only on submarine landslides as a tsunami generation mechanism, although the mechanical system described in Sect. 2 could conceivably be used to create a subaerial landslide.

Research concerning landslide-generated tsunamis has either concerned the replication of historical events or the modelling of an idealised scenario, in which the landslide is typically approximated as a solid block moving along a sloping boundary under the influence of gravity. Physical models are often used to validate mathematical models, which can subsequently be applied to field-scale events. Most experimental studies have used wave gauges to measure the free surface elevation (or run-up) at discrete locations within a tank or flume, providing only coarse data for model validation purposes. Mathematical models are able to provide complete spatial and temporal predictions of the generated waves, including the fluid kinematics if required. A combination of field investigations, mathematical modelling and physical experimentation is required to gain a thorough understanding of landslide-generated tsunamis. The remainder of this section describes the use of these three methods in the investigation of historical events and idealised scenarios, and the limitations associated with these studies.

1.2 Previous modelling of field events and idealised geometries

The Sissano Lagoon tsunami of 17 July 1998, which occurred shortly after a magnitude 7.1 earthquake, caused over 2200 casualties along a 40 km expanse of coastline. Field investigations identified wave heights in excess of 15 m at one location [14, 22], while distant tidal gauges in Japan recorded wave heights less than 20 cm [34]. The geographical concentration of the large waves suggested a local tsunami source in addition to the underwater fault rupture [31]; subsequent cruises by remotely-operated vehicles identified an underwater slump (rotational mass failure) capable of generating the large local wave heights [23]. Numerical modelling by Synolakis et al. [34] compared the wave heights generated by the underwater earthquake with those generated by a combined earthquake-

slump source. The combined source provided closer agreement with the spatial distribution, maximum amplitude and timing of the large wave impacts on the shoreline. The combination of field evidence and numerical modelling results supports a combined earthquake-slump tsunami source.

Although the Lituya Bay Tsunami of 10 July 1958 was generated by a subaerial landslide, the experimental techniques used to investigate the fluid kinematics in the landslide impact zone are directly relevant to the current study. The event is also of interest due to the extreme run-up of the waves on the opposite side of Gilbert Inlet, estimated to be approximately 524 m above sea level. Two- and three-dimensional experimental studies of the Lituya Bay Tsunami attempted to reproduce this wave run-up at laboratory scales [6]. A pneumatic landslide generator imparted motion to the granular slide, allowing realistic impact velocities to be achieved in the laboratory tests [3, 4]. This system could only be used for a subaerial landslide, as the generator motion would create spurious waves if used to create a submarine landslide. The run-up measured during these experiments corresponded to a field elevation of 526 m, while numerical model simulations with the multi-material hydrocode Impact Simplified Arbitrary Lagrangian Eulerian (iSALE) obtained a run-up prediction of 518 m [36]. The ability to control the landslide forcing clearly enabled successful reproduction of the run-up at laboratory scales; the current project applies a similar method to tsunamis generated by submarine landslides.

Possibly the simplest idealised geometry is created by modelling the landslide as a solid block moving along a horizontal bottom boundary under mechanical forcing [19]. Lee et al. [19] investigated the waves generated by a transcritical Froude number (defined in Eq. 2) block moving at a constant velocity, comparing the predictions of a Boussinesq and a KdV model with their shallow water experiments (using wave gauges to measure free surface elevations). In the transcritical range, their results identified precursor solitons propagating ahead of the disturbance and weakly-nonlinear weakly-dispersive trailing waves, and they recommend additional experimental investigations in the Froude number range $0.2 < Fr < 0.6$.

One variation of the idealised sloping-boundary geometry used in previous studies modelled the landslide as a solid triangular block sliding down a 45° slope [12]. Although this is geometry bears no resemblance to a field scenario, it has provided valuable insight into the wave generation and propagation processes. Watts [35] used the same two-dimensional experimental geometry to investigate the relative importance of dispersion and nonlinearity on the generated waves. Knowledge of the importance of dispersive and nonlinear effects is crucial to the useful simulation of these waves by numerical models. Watts found that waves generated by sufficiently long landslides on shallow slopes could be expected to behave as shallow water waves. If generated waves had an Ursell number of approximately 1, then initially linear waves would never exhibit nonlinear effects during their propagation. The Ursell number is defined as:

$$U \equiv \frac{a\lambda_d^2}{h^3}, \quad (1)$$

where h is the channel depth, a is the wave amplitude and λ_d is the dominant far-field wavelength. After validation against the wave amplitudes measured during the solid-block experiments of Heinrich [12], the Navier-Stokes solver Nasa-Vof2D predicted that the maximum wave amplitudes would decrease by approximately a factor of 2 when the solid block was replaced with a mass of sliding sand (of the same initial triangular geometry as the solid block). This implies that modelling a tsunamigenic landslide as a solid block is likely to over-estimate the amplitudes of the generated waves [29]. The block geometry

resulted in highly turbulent water motion in the vicinity of the landslide; this caused discrepancies between predictions of a smoothed particle hydraulics (SPH) model and the experimental measurements [27].

A boundary slope of 15° and a semi-elliptical landslide shape have been recommended by the tsunami research community as a benchmark configuration for experimental and numerical studies [8–10]. It should be noted that this benchmark scenario is still highly idealised compared to a field scenario, but is still valuable both for model validation purposes and to enable a thorough investigation into the wave generation and propagation. Jiang and Leblond [15–17] used a similar geometry to simulate the coupling between a deformable landslide and the generated waves. The interactions between the waves and the landslide were most significant for shallower submergence depths and lower landslide densities, although higher densities created larger waves. Sue et al. [32] measured both spatial and temporal variations in free surface elevation throughout a 15 m flume using the laser-induced fluorescence (LIF) technique. A boundary element method (BEM) model with linear free surface conditions predicted the maximum amplitudes recorded in these experiments to within $\pm 25\%$. Upon extending the benchmark experimental setup to include propagation in two horizontal dimensions, Enet and Grilli [2] confirmed Watts' finding that the landslide acceleration had a greater effect on the properties of the generated waves than its terminal velocity [35].

Most landslides occurring in the field are not infinite in their horizontal extent. Grilli et al. [8] observed quasi-2D behaviour in wave fields generated by landslides with *width : length* ratios larger than 2:1. Sammarco and Renzi [30] found that the location of the maximum wave amplitude on a shoreline occurred some distance away from the initial landslide location, due to dispersion in the longshore direction. Frequency dispersion was also important in determining the spatial variation of landslide tsunami run-up around a conical island [1, 28]. These results indicate that dispersive effects are more important for models considering propagation in two horizontal dimensions. Although three-dimensional models are more representative of field scenarios, two-dimensional models often allow the wave generation mechanism to be investigated in greater detail at significantly decreased cost.

1.3 Limitations of previous studies and project objectives

The problem geometry of a rigid block moving along a sloping boundary has several limitations. The use of a gravity control means that landslide motion may only be varied by changing either the landslide mass or slope angle. A sharp transition at the base of the slope could result in unrealistically sudden decelerations, while a gradual transition could cause aquaplaning of the landslide block [32]. Another problematic aspect of the sloping boundary is the inability to measure the properties of onshore-propagating waves. Waves generated by the motion of a landslide block propagate in both the onshore and offshore directions. Any waves propagating in the onshore direction would almost immediately interact with the sloping boundary, rendering their amplitude unable to be measured. Surface tension effects at laboratory scales can also affect run-up measurements (the only property of the onshore-propagating waves able to be effectively measured using this setup).

The present study investigates the properties of both offshore- and onshore-propagating waves generated by a submarine landslide. To achieve this, a series of two-dimensional experiments are undertaken with the solid block landslide moving along a horizontal bottom boundary, following the geometry of Lee et al. [19]. However, this study considers the effect of a landslide that accelerates to a constant velocity, moves at this constant

velocity for a short time and then decelerates to rest. Thus, the current study considers the relative importance of the different phases of motion on the generated waves, rather than using an acceleration-dominated sloping boundary geometry or neglecting the effects of the acceleration altogether.

Since the horizontal bottom boundary precludes the use of a shoreline within the problem domain, the offshore direction is defined as the direction of the landslide motion. The proposed experiments use a mechanical system to control the landslide motion, and the LIF technique of Sue et al. [32] to measure free surface elevations. This will provide a high-quality data-set with fine spatial and temporal resolution, unlike many previous studies which have relied on discrete free surface measurements, which can then be used to validate numerical models for this idealised scenario (complementing existing 2D and 3D experimental datasets used for this purpose). The landslide motion will be limited to relatively low Froude numbers, defined as:

$$Fr = \frac{u_t}{\sqrt{gD}}, \quad (2)$$

where u_t is the terminal landslide velocity, g is the gravitational acceleration and D is the water depth. The Froude number is therefore a measure of the terminal landslide velocity relative to the speed of a shallow water wave in water depth D . A low Froude number may be expected for a landslide moving down a relatively shallow slope.

The primary aims of the physical experiments are to repeatably generate, and accurately measure, waves over a horizontal boundary. Section 2 describes the experimental setup and measurement techniques used to achieve these aims. Section 3 discusses the ability of the mechanical system to achieve its motion targets in a repeatable manner, in addition to investigating the repeatability of the free surface measurements themselves. The primary purpose of this high-quality experimental data set is for the validation of numerical models. Section 4 describes two relatively simple inviscid-irrotational models which will be used for this purpose. Sections 5 and 6 describe the behaviour of the wave field, and assess the predictive capabilities of the two models over the parameter space. In particular, Sect. 6 will discuss the ability of the models to capture the energy in the offshore- and onshore-propagating wave groups, the phasing of the generated waves and the wave behaviour in the vicinity of the landslide.

2 Experimental method

2.1 Experimental setup

The current experiments were carried out in a flume of length 14.66 m, width 0.25 m and working depth 0.5 m, located within the Fluid Mechanics Laboratory of the Department of Civil and Natural Resources Engineering at the University of Canterbury, New Zealand. The working depth of the flume was reduced by 80 mm due to the installation of a false floor, so that the maximum submergence depth (above the false floor) tested in the flume was 350 mm. The water in the flume was pre-mixed with 0.1 mg/L of fluorescent Rhodamine B dye, to enable identification of the free surface using the LIF technique. The false floor in the flume provided the sliding surface upon which the landslide block moved, and was constructed from aluminium plate in the central 5 m of the flume and from 12 mm thick acrylic in the outer sections as shown in Fig. 1. During the experiments, the landslide block travelled only along the slotted central section of the false floor. The flume

boundaries were vertical walls without any wave absorption material, such that any waves reaching the ends of the flume were reflected back into the generated wave field. These reflections contaminated the generated wave field and effectively ended each experiment, as discussed in Sect. 5.

2.2 Landslide and mechanical system

The landslide was modelled as a semi-elliptical aluminium block, following the shape proposed in the benchmark configuration of Grilli et al. [7], and subsequently used by Sue et al. [32]. The block was 500 mm long, 250 mm wide and 26 mm thick, and was connected to the mechanical system beneath the false floor by an acrylic base plate. A recess in the base of the landslide block allowed the block to rest on the base plate with approximately 1 mm clearance from the sliding surface.

The base plate was connected to two toothed timing belts, located beneath the slotted sliding surface, by an aluminium I-section. Two teflon guides, passing through the slot at the front and back of the base plate, ensured that the landslide block did not lift off from the sliding surface at high velocities. The smaller toothed timing belt connected the mechanical system to the motor. The motor was a BL86-660 Watt brushless servo motor, of the kind used in computer numerical control (CNC) machines, driven by a Granite Devices VSD-E 160 drive system and controller. The drive system accepted input from a computer terminal, which specified motion as a text file containing a series of displacement-time targets. Each motor step was 1/4000th of a motor revolution, geared to provide a linear displacement resolution of 31,250 steps/m. A gantry, mounted on a rack-and-pinion system on the walls of the flume room, supported the lighting and image acquisition equipment; this allowed images to be recorded at any location along the length of the flume. A computer-controlled servo motor (of the same type as that used for the landslide mechanical system) provided the gantry motion, allowing repeatable horizontal positioning of the system to within ± 1 mm accuracy.

A preliminary series of particle tracking velocimetry (PTV) tests were undertaken to verify the ability of the mechanical system to achieve its motion targets in a repeatable manner. The landslide moved with a trapezoidal velocity profile in each experiment, consisting of three main phases of motion: an initial period of constant acceleration, a period of constant velocity, and a final period of constant deceleration to rest (at the same rate as the initial acceleration). The constant acceleration is a slight simplification of the tanh-type velocity profile used by Pelinovsky and Poplavsky [26], allowing classification of the acceleration phase of motion with a single parameter, while the deceleration is an

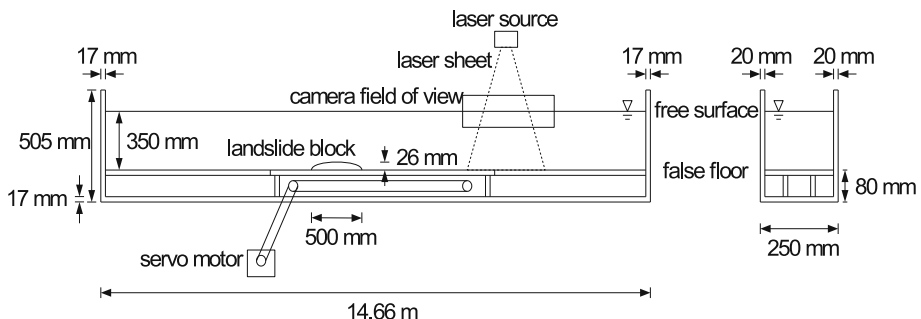


Fig. 1 Setup used in current experimental study

obvious requirement of a physical experiment in a finite-length flume. Three white dots (approximately 3 mm in diameter) were painted onto the side of the black landslide block, and a JAI M4⁺ CL camera outside of the flume recorded their motion at 70 Hz. The camera images were 1380 pixels wide and 256 pixels high, with a spatial resolution of 0.305 mm/pixel. Since the horizontal extent of the camera field of view was approximately 350 mm, each experiment was repeated several times to measure the entire landslide motion. The camera records were synchronised using a light-emitting diode (LED) within the image, which flashed for approximately 0.1 s upon initiation of landslide motion. The Streams software package [25] carried out a PTV analysis to determine the displacements and Lagrangian velocities of each of the dots on the landslide. Section 3 describes the results of these preliminary landslide motion experiments.

2.3 Free surface identification

The experiments used an application of the LIF technique [32] to achieve accurate identification of the spatial and temporal variations in the free surface elevation caused by the landslide motion. During an experiment, the solid state laser illuminated a plane section of the flume from above, with a power level of approximately 600 mW (at 532 nm). The Rhodamine dye fluoresced under the laser light, allowing identification of the free surface as the interface between the fluorescing water and the dark air above. The camera (details are provided in Sect. 2.2) captured images of the free surface motion at 70 Hz during each experiment. The camera was located 2.1 m from the flume sidewall, and captured images at an angle of 5° downwards from the horizontal to ensure that measurements were not affected by the fluid meniscus at the sidewall. Each experiment was repeated 37 times to capture data over the length of the flume; the combination of records from different gantry locations placed strict requirements on the repeatability of the generated waves (and hence on the landslide motion). The gantry system moved 350 mm between each experiment, providing approximately 50 mm overlap between the recorded images. An LED again synchronised the image records in time.

The image processing method was based on the work of Sue et al. [32]; this method is described in detail in [37], with the main steps summarised below. The Streams software package [25] produced the pixel intensity field for each image. The intensity field associated with each camera location was output as a text file for subsequent processing. The free surface record associated with each intensity field was calculated separately using Matlab; the free surface records over the flume length were then combined to obtain the total free surface record for that experiment. At each camera location, the free surface identification algorithm calculated the unique threshold intensity associated with each x - t location within the record. Due to spatial and temporal variations in the laser intensity, and hence in the intensity of light emitted by the fluorescing dye, a single threshold value was not possible (as used by Sue et al. [32]). The algorithm instead identified the upper and lower limits of the free surface, and calculated the threshold intensity as:

$$I_t = 0.6(I_1 - I_0) + I_0, \quad (3)$$

where I_0 is the low intensity at the upper edge of the interface (air), I_1 is the high intensity at the lower edge of the interface (water), and I_t is the threshold intensity. The algorithm then interpolated between pixels on the interface to determine the location of the free surface to sub-pixel accuracy. Although the joins in the flume sidewall were transparent (i.e. no steel frame encased the flume sidewalls), the free surface could not be identified within these regions. At each time within the record, the algorithm interpolated over these

joins to create a continuous free surface record over the length of the flume. The algorithm also corrected for the gantry angle and elevation (which were prone to small variations, due to the rack and pinion system) before combining the records from different camera locations.

3 Landslide motion

As discussed in Sect. 2, highly repeatable landslide motion was required to ensure that LIF measurements at different locations along the flume could be combined. To achieve this, a series of PTV experiments provided measurements of the displacements and Lagrangian velocities of three dots painted on the side of the landslide block. This section compares the recorded landslide motion to the targets used by the mechanical system. Six experiments were conducted over a range of landslide accelerations (defined as a_0) and terminal velocities (defined as u_t), as summarised in Table 1. These experiments used a water depth of 175 mm to limit the total distance travelled by the landslide, and hence the required number of experimental repetitions. Although the motion checks were not repeated at a depth of 350 mm, the wave field data obtained from these experiments (discussed in Sect. 6) indicated excellent repeatability of the motion.

The mechanical system reproduced the target trapezoidal velocity profile accurately, as shown in Fig. 2 for three repetitions of an experiment with an initial acceleration of 1.0 m/s^2 and a terminal velocity of 328 mm/s (Run 4). The displacements and velocities of the individual particles on the side of the landslide were averaged for each experiment, to reduce errors caused by the particle identification process (discussed below). The velocity of the landslide exhibited some variation, most obviously during the constant-velocity phase of motion. The root-mean squared (RMS) error in the constant-velocity landslide motion was 7.3 mm/s for this experiment. Equivalent RMS errors over the range of PTV experiments are provided in Table 1. As the landslide terminal velocity increased, the RMS error decreased as a percentage of the landslide terminal velocity (although the absolute RMS error increased). Uncertainties in the identification of the particle location and the time of image capture led to uncertainties in the displacements and velocities of the landslide. As stated in Sect. 2, the camera captured images at a rate of 70 frames/s with a resolution of 0.305 mm/pixel. Assuming that the location of each particle was correctly identified to within ± 0.5 pixels, this gives a possible displacement error of ± 0.15 mm and a possible velocity error of ± 10.7 mm/s. The RMS errors in the terminal landslide velocity were less than this value. The agreement between the three repeated experiments in Fig. 2 was excellent during the acceleration and deceleration phases of motion, and the scatter during the constant-velocity motion was consistent in all three repeats.

Table 1 RMS errors in landslide motion

Run	a_0 (mm/s ²)	u_t (mm/s)	u_{RMS} (mm/s)	u_{RMS} (% of u_t)
1	500	164	6.2	3.8
2	500	328	7.7	2.3
3	1000	164	6.7	4.1
4	1000	328	7.3	2.2
5	1500	164	6.8	4.2
6	1500	328	7.1	2.2

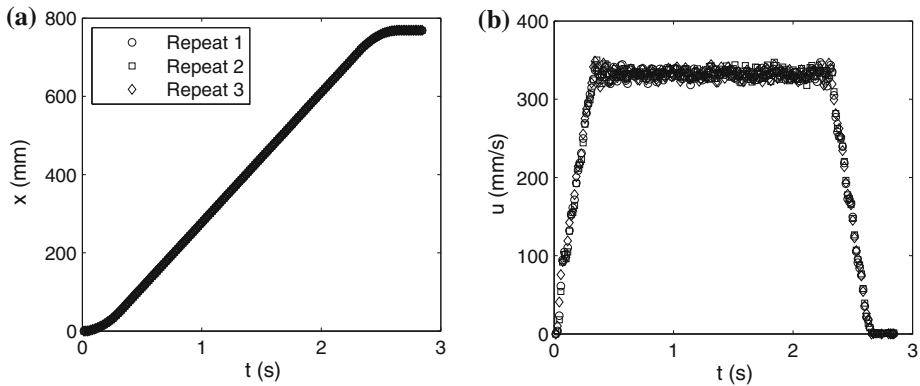


Fig. 2 Repeatability checks on the landslide **a** displacement, and **b** velocity for a trapezoidal motion profile with $a_0 = 1.0 \text{ m/s}^2$, $u_t = 328 \text{ mm/s}$, at a submergence depth of $D = 175 \text{ mm}$

To check the repeatability of the free surface waves generated by the landslide motion, a single LIF experiment was repeated four times using the same camera location. Figure 3 shows the time series of the identified free surface elevation at one horizontal location within the image. The noise in the free surface record is of $O(0.1 \text{ mm})$, and the measurements of the free surface were therefore repeatable to sub-pixel accuracy.

4 Model description

As discussed in Sect. 1, the primary motivation for the physical experiments of this paper is to provide a high-quality dataset for the validation of numerical models based on the idealised scenario of a rigid block and horizontal seafloor. This section describes the key

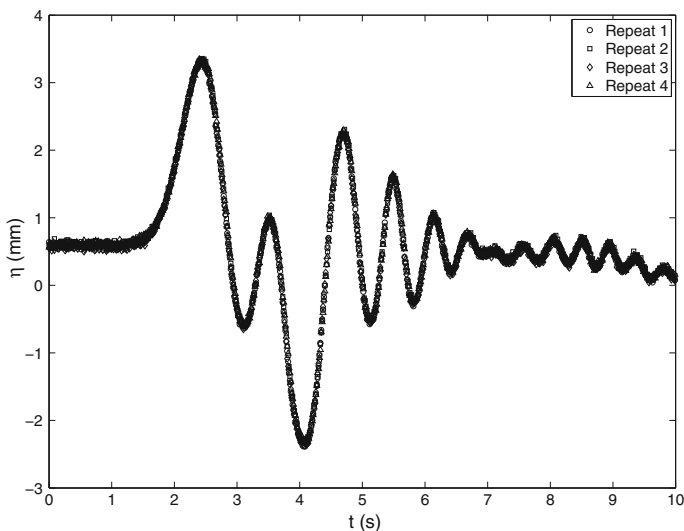


Fig. 3 Repeatability checks on generated wave field, for a trapezoidal motion profile with $a_0 = 1.0 \text{ m/s}^2$, $u_t = 0.328 \text{ m/s}$, and a submergence depth of $D = 0.175 \text{ m}$

features of two simple inviscid-irrotational models used to predict the waves generated by the landslide motion. The first of these models invokes the linear assumption on the bottom boundary and on the free surface, and is solved by a spectral decomposition of wave modes [33, 37]. The second model is a BEM model, and uses the full bottom boundary condition in conjunction with the assumed linear free surface condition, described in [32]. The wave fields predicted by these models are compared to the LIF measurements in Sect. 6.

Figure 4 illustrates the problem domain for both of these models. The solid block landslide moves along the horizontal boundary in the positive x -direction, generating waves on the free surface of the fluid. Although the domain is assumed infinite in horizontal extent, in reality the wave field will be periodic in x depending on the wavenumber resolution Δk . In these simulations, this resolution was set so that none of the repeated waves entered the simulation domain. The origin of the coordinate system is located on the undisturbed free surface, directly above the initial position of the landslide centre of mass. The bottom boundary, $y = y_b$, includes the shape of the landslide, such that:

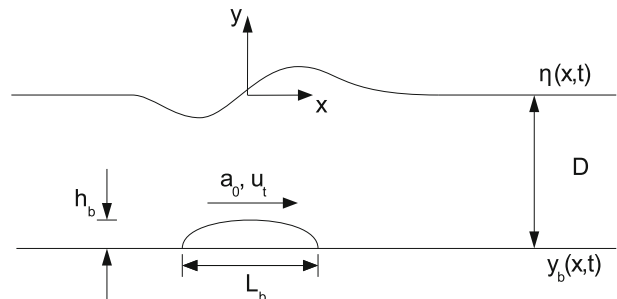
$$y_b = -D + h_b f(\theta(x, t)), \quad (4)$$

where $f(\theta)$ is the landslide shape function and $\theta(x, t) = x - x_0(t)$ is the horizontal coordinate relative to the landslide centre of mass, $x_0(t)$.

The governing equation for both models is Laplace's equation for the velocity potential, and both models use the linearised kinematic and dynamic conditions on the free surface of the fluid; this assumption is stated by Lee et al. [19] to be valid up to a Froude number of approximately 0.2. The linear model also invokes the linear assumption on the bottom boundary, assuming that the landslide thickness (h_b) is very small compared to both the landslide length (L_b) and the fluid depth (D). Under this assumption, the moving landslide imparts a vertical velocity to the fluid on the boundary. The nonlinear model includes the nonlinear flow tangency condition on the bottom boundary. The initial conditions of the models require zero velocity potential and an undisturbed free surface throughout the model domain.

The two models are most conveniently solved in nondimensional form. Horizontal and vertical distances in the models are nondimensionalised by the length of the landslide, L_b . The length scale assigned to perturbations (the time-dependent bottom boundary y_b and the free surface elevation η) is the landslide thickness, h_b . Times within the models are nondimensionalised by $\sqrt{g/L_b}$. Thus, the nondimensional variables used in the models are:

Fig. 4 Simulation domain used by inviscid-irrotational models in this study



$$x' = \frac{x}{L_b}, y' = \frac{y}{L_b}, y'_b = \frac{y_b}{h_b}, t' = t\sqrt{\frac{g}{L_b}}, \eta' = \frac{\eta}{h_b}, \phi' = \frac{\phi}{h_b\sqrt{gL_b}}, k' = kL_b, \omega = \omega\sqrt{\frac{L_b}{g}}, \quad (5)$$

where k is the wavenumber and ω is the angular frequency of the generated waves. Other variables are defined in Fig. 4. The experimental measurements presented in Sects. 5 and 6 will be nondimensionalised in the same manner, and nondimensional variables will be used in the remainder of this paper unless otherwise stated (with primes dropped for convenience). This nondimensional formulation introduces three nondimensional parameters concerning the landslide motion and the ambient fluid depth. These three parameters are:

$$\tau = \frac{D}{L_b}, \lambda = \frac{a_0}{g}, Fr = \frac{u_t}{\sqrt{gD}}, \quad (6)$$

where τ is the nondimensional fluid depth, λ is the nondimensional landslide acceleration, and Fr is the nondimensional terminal velocity of the landslide (also defined in Eq. 2).

The assumed solution form used within the linear model is based on the solution of Lighthill [20] for the waves generated by objects in a steady stream. The assumed solutions for the velocity potential and the free surface elevation are:

$$\phi(x, y, t) = \int_{-\infty}^{\infty} e^{i(kx - \omega t)} [a(k, t) \cosh k(y + \tau) + b(k, t) \sinh k(y + \tau)] dk, \quad (7)$$

and

$$\eta(x, t) = \int_{-\infty}^{\infty} e^{i(kx - \omega t)} c(k, t) dk, \quad (8)$$

where $a(k, t)$, $b(k, t)$ and $c(k, t)$ are the spectral coefficients associated with the velocity potential and the free surface elevation. Only the real parts of these solutions are required.

Upon application of the boundary conditions to the solution form of Eqs. 7 and 8, the spectral coefficients $c(k, t)$ are obtained for each k value by solving the ordinary differential equation:

$$\frac{d^2 c}{dt^2} - 2i\omega \frac{dc}{dt} + G(k, t) = 0, \quad (9)$$

where $G(k, t)$ is the wave forcing function due to the landslide motion:

$$G(k, t) = \frac{e^{i(\omega t - kx_0)} p(k)}{\cosh(k\tau)} \left[\frac{d^2 x_0}{dt^2} - ik \left(\frac{dx_0}{dt} \right)^2 \right]. \quad (10)$$

The calculation of the wave field in the linear model is therefore achieved in two steps. Firstly, Eq. 9 is solved for the spectral coefficients $c(k, t)$, and secondly these coefficients are then integrated over wavenumber space according to Eq. 8.

The nonlinear model solves Laplace's equation on the boundaries of the domain using a boundary element method (BEM) formulation. As discussed above, the model uses the nonlinear bottom boundary condition. For further details on the full solution process, and the application of this model to a sloping boundary, see Sue et al. [32].

5 Wave field properties

Although the properties of the generated waves were strongly dependent upon the motion of the landslide, the general evolution of the wave field was similar in all of the experiments undertaken at low Froude numbers. This section discusses the wave generation and propagation within a representative experiment, with the nondimensional parameters $\lambda = 0.153$, $Fr = 0.25$ and $\tau = 0.35$. These parameters (defined in Eq. 6) corresponded to an initial landslide acceleration of 1.5 m/s^2 , a terminal landslide velocity of 328 mm/s and a submergence depth of 175 mm . The measured wave amplitudes were nondimensionalised by the landslide thickness, as discussed in Sect. 4.

Figure 5 shows a two-dimensional plot of the wave amplitudes generated by the landslide motion during this experiment. The horizontal axis represents the nondimensional distance along the flume with respect to the initial location of the landslide centre of mass, the vertical axis represents the nondimensional time since the initiation of the landslide motion, and the colour scale represents the wave amplitude. The diagonal colour bands thus correspond to the characteristic curves of the generated waves in the x - t plane. During this experiment, the maximum wave amplitude was approximately 0.18 in nondimensional terms, corresponding to a maximum dimensional amplitude of approximately 4.5 mm .

The landslide initially accelerated at a constant rate until $t = 0.97$. This initial acceleration generated a leading offshore-propagating crest and onshore-propagating trough, both of which were followed by trailing packets of waves that resemble the Airy wave solution discussed by Mei et al. [24]. Although not strictly shallow water waves, which implies propagation without changing form and wavelengths greater than 20 times the water depth, the leading waves approached the behaviour of shallow water waves. The

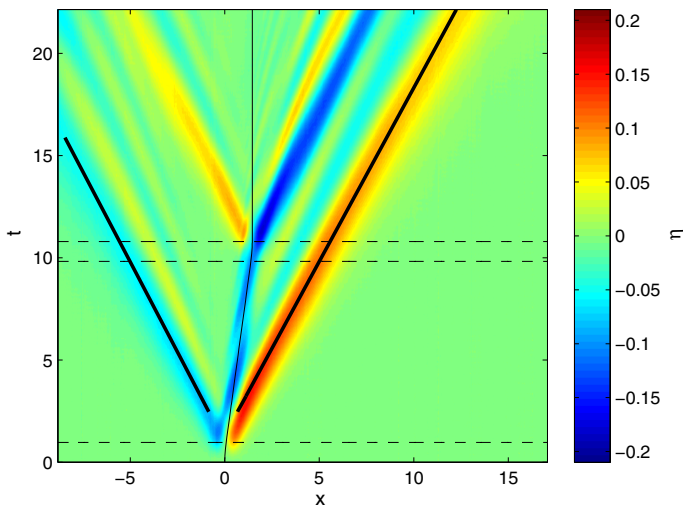


Fig. 5 Contour plot of wave amplitudes generated during an experiment with the nondimensional parameters $\lambda = 0.153$, $Fr = 0.25$ and $\tau = 0.35$. The *solid black line* represents the location of the landslide centre of mass, and the *dashed horizontal lines* represent the times at which the landslide motion changed from constant acceleration to constant velocity ($t = 0.97$), constant velocity to constant deceleration ($t = 9.83$), and constant deceleration to rest ($t = 10.80$). The *thick black lines* show the characteristic curves of the leading waves

characteristic curves of the leading waves, based on a linear fit to the location of the maximum crest elevation (or trough depression), are shown in Fig. 5. The phase velocities calculated based on the crest and trough characteristic curves were approximately 99 and 95 % of the shallow water wave speed for this depth. The trailing waves had much shorter wavelengths, and their dispersive properties are clearly visible in Fig. 5. The dispersive nature of these waves indicates that shallow water (non-dispersive) models will not correctly predict the properties of waves generated during these experiments, and should be applied to submarine landslide-generated tsunamis with caution.

The high velocity of the fluid moving over the landslide during its constant-velocity motion created a low-pressure region above the landslide. The free surface became depressed above this low-pressure region, shown by the dark blue region above the moving landslide in Fig. 5. The free surface depression is similar to that created by a subcritical open channel flow over a submerged hump, although the relatively short flume length and finite duration of the constant-velocity motion limit the applicability of this analogy. This depression is also predicted by the weakly dispersive models of Lee et al. [19]. Unlike their predictions, however, the depressed region observed in the current experiments did not extend beyond the landslide. The terminal landslide velocity was lower than the phase velocities of the offshore-propagating waves, and so successive crests and troughs passed over the landslide during its constant-velocity motion. The free surface depression decreased the amplitude of crests, and increased the amplitude of troughs, passing over the landslide.

The landslide deceleration generated two additional dispersive wave packets, similar to those generated by the initial landslide acceleration. The offshore-propagating packet contained a leading trough, while the onshore-propagating packet contained a leading crest. Again, the behaviour of these leading waves approached the shallow water limit. Once the landslide began its deceleration, the free surface depression generated during its constant-velocity motion propagated in the offshore direction as a free trough.

Due to the fully reflective flume boundaries (see Sect. 2), the waves were reflected back into the wave field upon reaching the ends of the flume. The leading onshore-propagating trough reached the end of the measurement zone at approximately $t = 7$, and was reflected soon after this time (although the reflected amplitudes were very small

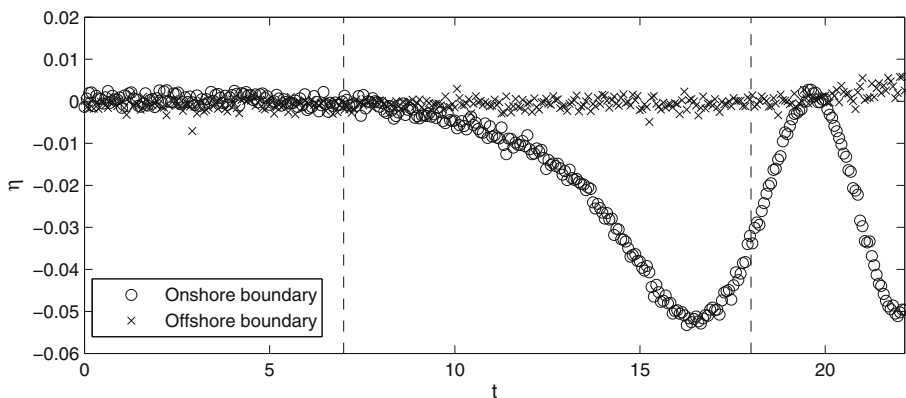


Fig. 6 Free surface elevation time series at the onshore and offshore ends of the flume, showing the times at which waves reached the flume ends (and were subsequently reflected)

initially). The leading offshore-propagating crest reached the offshore end of the measurement zone at approximately $t = 18$. Figure 6 shows the arrival of these waves at the onshore and offshore ends of the flume. These reflected waves affected the calculation of bulk quantities (such as the energy within the wave field) from the experimentally-measured wave amplitudes.

6 Wave field behaviour for low-Fr landslide forcing

6.1 Dependence of wave field on landslide Froude number

In the current experiments, the landslide Froude number had a greater effect on the wave field evolution than the landslide acceleration or submergence depth. Only sub-critical landslide Froude numbers were tested, and a low Froude number is defined in this study as $Fr < 0.5$. Table 2 contains the nondimensional parameters tested within this study, where t_1 , t_2 and t_3 were the nondimensional times of motion change (shown in Fig. 5). The constant-velocity phase of motion had the same duration in all of the experiments. Non-linear effects became dominant within the wave field at higher Froude numbers, altering the behaviour of the entire wave field. These high-Fr effects will be the focus of a subsequent paper.

The effects of changing Froude number upon the wave field may be assessed by comparing the magnitude and spatial distribution of the wave amplitudes within different experiments. However, comparisons over the entire wave field may also be obtained using the potential energy within the wave field. This potential energy of the nondimensional wave field is defined as:

Table 2 Experimental parameters for low-Froude number experiments

Run no.	Fr	λ	τ	t_1	t_2	t_3
1	0.125	0.051	0.70	2.05	10.91	12.96
2	0.125	0.051	0.35	1.45	10.31	11.76
3	0.125	0.102	0.70	1.03	9.89	10.91
4	0.125	0.102	0.35	0.73	9.58	10.31
5	0.125	0.153	0.70	0.68	9.54	10.23
6	0.125	0.153	0.35	0.48	9.34	9.83
7	0.250	0.051	0.70	4.10	12.96	17.07
8	0.250	0.051	0.35	2.90	11.76	14.66
9	0.250	0.102	0.70	2.05	10.91	12.96
10	0.250	0.102	0.35	1.45	10.31	11.76
11	0.250	0.153	0.70	1.37	10.23	11.60
12	0.250	0.153	0.35	0.97	9.83	10.79
13	0.375	0.051	0.70	6.16	15.02	21.17
14	0.375	0.051	0.35	4.35	13.21	17.56
15	0.375	0.102	0.70	3.08	11.94	15.02
16	0.375	0.102	0.35	2.18	11.04	13.21
17	0.375	0.153	0.70	2.05	10.91	12.96
18	0.375	0.153	0.35	1.45	10.31	11.76

$$E_P(t) = \frac{1}{2} \int_{-\infty}^{\infty} \eta(x, t)^2 dx, \quad (11)$$

where all quantities are in their nondimensional form. The dimensional form of this equation is the standard equation for the potential energy within a wave field:

$$E_P(t) = \frac{1}{2} b \rho_w g \int_{-\infty}^{\infty} \eta(x, t)^2 dx, \quad (12)$$

where b is the flume width, ρ_w is the density of water and g is the gravitational acceleration. Unlike the corresponding equation used to determine the potential energy from a discrete free surface elevation time series [5], this equation does not need to be calculated for separate waves assuming that each wave propagates at a constant velocity. Figure 7 illustrates the effect of the landslide Froude number on the generated wave amplitudes, and hence on the potential energy within the wave field, for experiments conducted with a nondimensional landslide acceleration of $\lambda = 0.153$ and a submergence depth of $\tau = 0.35$. The three contour plots show the same general behaviour discussed in Sect. 5, with the landslide acceleration and deceleration generating packets of onshore- and offshore-propagating waves. The constant-velocity motion of the landslide influenced the offshore-propagating waves, leading to significant differences in behaviour between the three experiments.

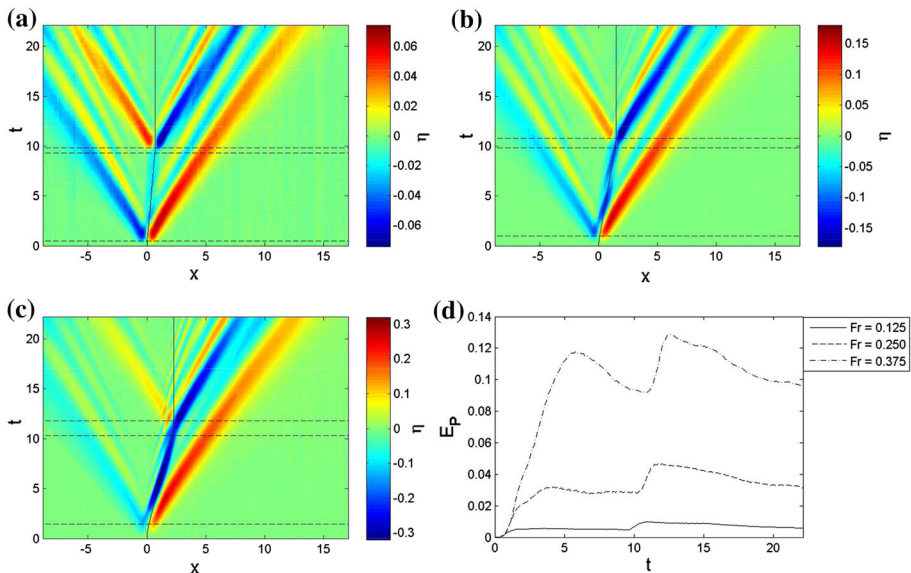


Fig. 7 **a** Wave field contour plot for an experiment with the parameters $\lambda = 0.153$, $\tau = 0.35$, and $Fr = 0.125$, **b** Wave field contour plot for an experiment with the parameters $\lambda = 0.153$, $\tau = 0.35$, and $Fr = 0.250$, **c** Wave field contour plot for an experiment with the parameters $\lambda = 0.153$, $\tau = 0.35$, and $Fr = 0.375$, **d** Potential energy time series for experiments conducted with $\lambda = 0.153$ and $\tau = 0.35$. In the contour plots, the *solid black line* represents the location of the landslide centre of mass, and the *dashed horizontal lines* represent the times of landslide motion change

Increasing the Froude number increased the maximum amplitudes of the waves generated during an experiment. At the lowest Froude number of 0.125, the short duration of the landslide acceleration meant that the amplitudes of the onshore- and offshore-propagating waves were approximately equal when the landslide reached its terminal velocity. Since this terminal velocity was low compared to the celerity of the offshore-propagating waves, these waves passed over the landslide with minimal interaction. Additionally, the free surface depression above the landslide had a negligible amplitude. Thus, the wave field was dominated by the waves generated by the landslide acceleration and deceleration.

As the Froude number increased, the increased duration of the landslide acceleration led to larger wave amplitudes within the offshore-propagating packet. The landslide also exhibited stronger interactions with the offshore-propagating waves during its constant-velocity motion. The free surface depression above the landslide, barely noticeable at the lower Froude numbers, had a larger amplitude than the leading waves at $Fr = 0.375$. The amplitude of this depression fluctuated as successive crests and troughs passed over the landslide. At $Fr = 0.375$, the relatively high landslide velocity appeared to increase the amplitudes of the offshore-propagating waves behind the landslide while decreasing the amplitudes of those waves passing over the landslide.

The time series plot of Fig. 7d shows the effect of increasing the landslide Froude number on the potential energy within the entire wave field. The initial rate of energy increase was the same in the three experiments, although the different durations of the acceleration period led to substantial differences in the maximum potential energy within the wave field. At the lowest Froude number, the negligible interactions between the landslide and the offshore-propagating waves caused the potential energy to remain approximately constant throughout the constant-velocity phase of motion. As the Froude number (and hence, the size of these interactions) increased, the amplitude and period of the energy fluctuations during the constant-velocity phase also increased. The waves generated by the landslide deceleration caused an additional increase in the potential energy within the wave field.

The potential energy calculation of Eq. 11 may also be applied to different regions of the wave field to estimate the energy within the offshore- and onshore-propagating wave packets. This is a simplistic approach of estimating the energy within the wave packets, since the onshore-propagating packet may not have been entirely located within the

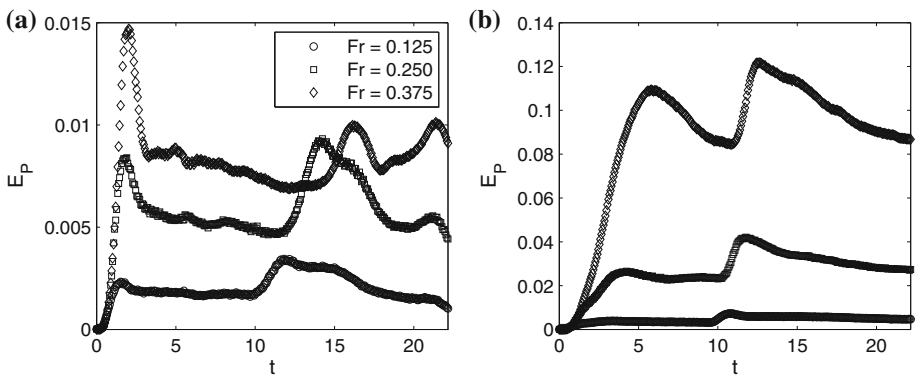


Fig. 8 Dependence of potential energy within the **a** onshore and **b** offshore regions on the landslide Froude number, for experiments carried out with $\lambda = 0.153$ and $\tau = 0.35$

onshore region (particularly after the landslide began its acceleration or deceleration). However, this approach provides a reasonable estimate of the energy contained within the two wave groups during the constant-velocity landslide motion. Figure 8 shows the potential energy contained within the onshore (negative- x) and offshore (positive- x) regions of the flume for the three Froude numbers. Clearly, the energy in the offshore region was much larger than in the onshore region, and exhibited greater dependence on the landslide Froude number. The effect of reflections on the energy within the onshore region is also evident after approximately $t = 10$.

In addition to the potential energy, the full spatial and temporal resolution of the generated wave field also allows calculation of the nondimensional mass within the wave field, according to:

$$m(t) = \int_{-\infty}^{\infty} \eta(x, t) dx. \quad (13)$$

In a series of inviscid-irrotational simulations with linear free surface conditions, Sue [33] observed that the offshore- and onshore-propagating wave packets generated during the landslide acceleration and deceleration contained positive and negative mass respectively. Although the total mass in the model domain remained constant, mass was directionally transported in these wave packets—an unexpected result for a linear wave model. Figure 9 shows the mass within the offshore and onshore regions of the flume for experiments conducted at Froude numbers of 0.125, 0.250 and 0.375 (with $\lambda = 0.153$ and $\tau = 0.35$). The mass within these two regions approximates the mass contained within the offshore- and onshore-propagating wave groups, in a similar manner to the potential energy (discussed above). In addition to confirming the directional mass transport predicted by Sue [33], Fig. 9 shows that this mass transport increased with the landslide Froude number. Although reflections of the onshore-propagating waves affected the mass calculations at later times, the division between onshore and offshore mass is clear. The waves generated by the landslide deceleration effectively cancelled out the directional mass transport.

Based on these results, the landslide Froude number affected the wave field in two main ways. Firstly, the duration of the landslide acceleration scaled with the Froude number, affecting the amplitudes (and the associated energy and mass) of the offshore- and

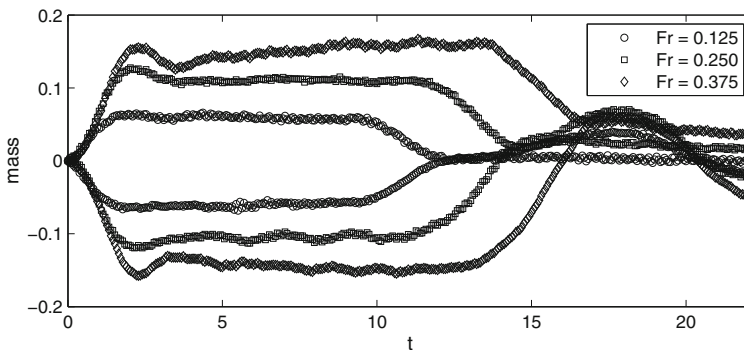


Fig. 9 Froude number dependence of mass within the wave field, for experiments carried out with $\lambda = 0.153$ and $\tau = 0.35$

onshore-propagating wave packets. Secondly, the terminal velocity of the landslide determined the level of interaction between the landslide and the offshore-propagating waves. At higher landslide Froude numbers, the constant-velocity phase of motion had a greater effect on the wave field evolution than the acceleration or deceleration phases. Section 6.4 discusses the application of these results to previous sloping-boundary studies.

6.2 Effect of landslide acceleration and submergence depth

The effects of the submergence depth and landslide acceleration on the generated wave field are discussed in this section, considering a landslide Froude number of 0.25. Figure 10 illustrates the effect of both landslide acceleration and submergence depth on the generated waves, considering the minimum and maximum landslide accelerations ($\lambda = 0.051$ and 0.153) only.

The generated waves had lower amplitudes at the deeper submergence depths than at the shallower submergence depths. The wavelengths (and hence propagation velocities) of the generated waves were larger in the deeper experiments. These results are consistent with the findings of previous sloping-boundary experiments, where shallower initial landslide submergence depths led to the generation of larger-amplitude waves [32, 35]. However, the submergence depth had a negligible effect on the behaviour of the wave field. This is evident from the qualitative similarity of Fig. 10a, b for $\lambda = 0.51$, and of Fig. 10c, d for $\lambda = 0.153$. In both cases, the wave field evolved in an almost identical manner despite differences in the amplitude and wavelength of the generated waves.

Increasing the landslide acceleration by a factor of 3 had a similar effect on the maximum wave amplitudes as decreasing the submergence depth by a factor of 2. However, the

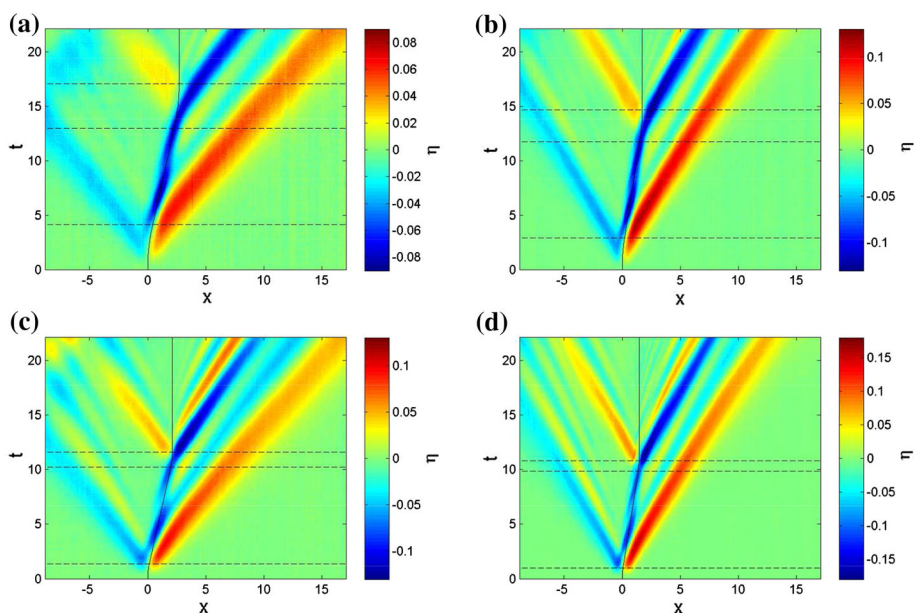


Fig. 10 Wave field contour plots for experiments carried out with $Fr = 0.25$, and **a** $\lambda = 0.051$, $\tau = 0.70$, **b** $\lambda = 0.051$, $\tau = 0.35$, **c** $\lambda = 0.153$, $\tau = 0.70$, **d** $\lambda = 0.153$, $\tau = 0.35$. The solid black line represents the location of the landslide centre of mass, and the dashed horizontal lines represent the times of landslide motion change

landslide acceleration had a greater effect than the submergence depth on the overall behaviour of the wave field. The leading waves generated by the landslide acceleration were more pronounced at the lower landslide accelerations, while the while the dispersive trailing wave packets were relatively more prominent at the higher accelerations. This implies that a field landslide with a short, sharp landslide acceleration may generate a wave packet with a greater distribution of energy throughout its wavelengths. The effect of the landslide acceleration on the dispersive trailing waves was most evident in the onshore-propagating wave packet.

In addition to these effects on the onshore- and offshore-propagating wave packets, the landslide acceleration modified the interactions between the landslide and the offshore-propagating waves during the constant-velocity phase of motion. When moving with a higher initial acceleration, the landslide reached its terminal velocity sooner relative to the timescale of the wave propagation. Thus, the landslide was located closer to the front of the offshore-propagating wave packet when it began its constant-velocity motion, so that more waves passed over the landslide during this phase of motion. Since the larger landslide acceleration also produced large trailing waves (relative to the size of the leading wave), these waves had a greater effect on the amplitude of the free surface depression above the landslide. Thus, the fluctuations in the depression amplitude were larger for the higher landslide acceleration. Although the landslide Froude number had the most pronounced effect on the behaviour of the generated wave field, the landslide acceleration could alter this behaviour slightly by affecting the interaction between the landslide and the trailing waves.

Figure 11 shows the effect of the landslide acceleration and submergence depth on the potential energy and mass within the generated wave field. The potential energy within the wave field increased most rapidly for the high landslide acceleration and shallow submergence depth; this rate of energy increase exhibited a stronger dependence on the acceleration than the submergence depth. However, the landslide submergence depth had a greater effect on the maximum potential energy within the wave field. The maximum masses within the offshore and onshore regions of the wave field were approximately equal for all of these experiments, demonstrating that the directional mass transport only depended on the landslide Froude number. The initial increase in mass within the offshore region, and corresponding decrease in mass within the onshore region, exhibited dependence on both the landslide acceleration and submergence depth. The rate of mass increase

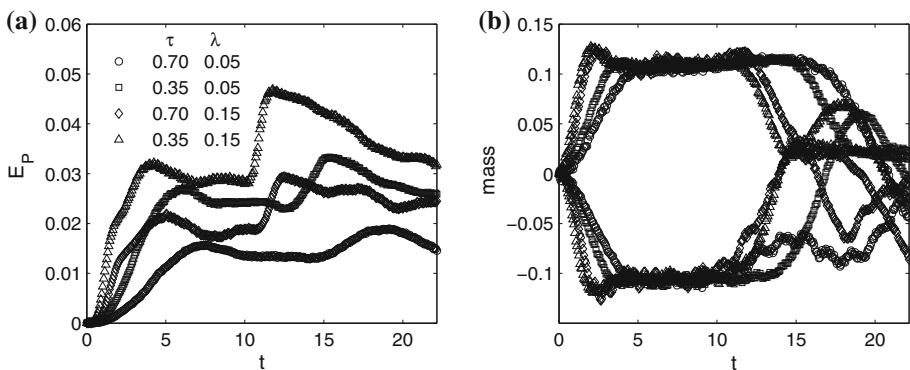


Fig. 11 **a** Potential energy and **b** mass dependence on landslide acceleration and submergence depth, for experiments carried out with $Fr = 0.25$

(in absolute terms) was highest for the larger landslide acceleration and shallower submergence depth.

6.3 Predictive capabilities of inviscid-irrotational models

This section compares the predictions of the two inviscid-irrotational models to the LIF measurements. These models are able to capture the dispersive characteristics of the generated waves, unlike a shallow water model, however the linearised free surface boundary conditions limit the applicability of the models to low wave steepnesses. Hence, it may be expected that the model performance will worsen as the landslide Froude number (and initial acceleration, to a lesser extent) increases, or as the submergence depth decreases. The model with the fully nonlinear bottom boundary condition is also expected to provide more robust predictions of the generated wave field. The predictive capabilities of the two models are assessed over the range of landslide Froude numbers, for experiments with $\lambda = 0.153$ and $\tau = 0.35$. This combination of landslide acceleration and submergence depth generated the steepest waves at each Froude number (as discussed in Sect. 6.2), and will therefore provide an effective test of the model predictions.

Due to the different landslide Froude numbers used in the three experiments, the model predictions differed during the constant-velocity phase of motion. Figure 12 compares the predicted and measured wave fields at $t = 8.0$, which was during the constant-velocity phase of motion for the three experiments. At this time, the onshore-propagating wave packet propagated without significant interaction with the moving landslide. Hence, comparisons between the measured and predicted onshore-propagating waves may indicate the effectiveness of the models at predicting waves generated by the landslide acceleration. Both models correctly predicted the phasing of the onshore-propagating waves. The linear model slightly under-predicted the amplitude of all of the onshore-propagating waves, while the nonlinear model slightly over-predicted the amplitude of the leading trough and under-

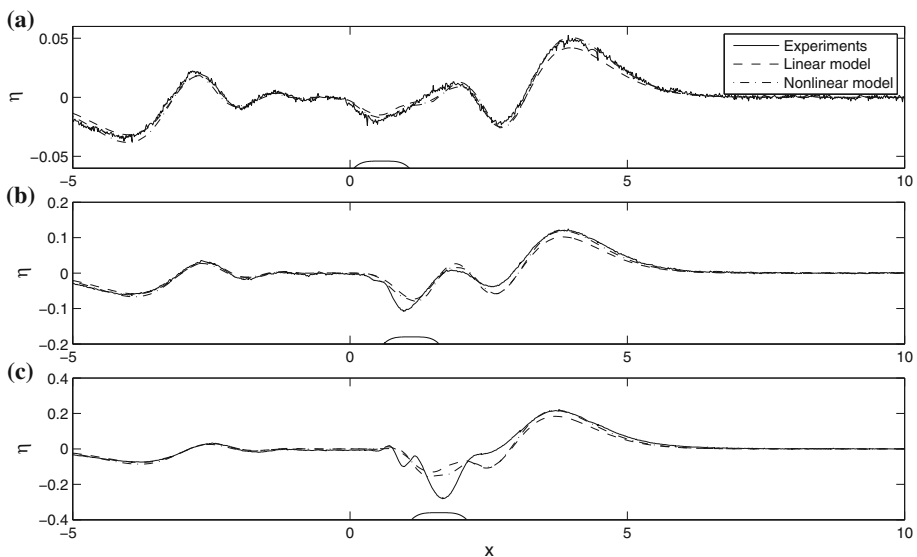


Fig. 12 Predictive capabilities of numerical models for experiments with $\lambda = 0.153$ and $\tau = 0.35$ and **a** $Fr = 0.125$, **b** $Fr = 0.250$, **c** $Fr = 0.375$. The predicted and measured wave fields are compared at $t = 8.0$

predicted the trailing wave amplitudes. Thus, inclusion of the fully nonlinear bottom boundary condition improved the model predictions of the waves generated by the landslide acceleration. The initial under-predictions of the leading wave amplitude are more apparent when considering the potential energy within the wave field (discussed below).

As the leading crest and trough propagated along the flume, the experimentally-measured waves decreased in amplitude more rapidly than the predicted waves. Figure 13 illustrates this amplitude decay for the envelope of the leading offshore-propagating crest, nondimensionalised by the amplitude of the envelope at $x = 4$. The crests predicted by the models both decayed slightly more slowly than the $x^{-1/3}$ law used for the far-field amplitude of a tsunami wave in the absence of lateral dispersion [18, 24]. However, the experimentally-measured leading crest decayed more rapidly than predicted by this power law. This may be due to energy losses caused by sidewall friction or turbulence, neither of which are accounted for by the inviscid-irrotational models.

The leading offshore-propagating crest also exhibited minimal interaction with the landslide during the constant-velocity phase of motion, and the linear and nonlinear models under-predicted and over-predicted the amplitude of this wave, respectively. However, the other waves within the offshore-propagating packet did interact with the landslide during this phase of motion. At the lowest Froude number of 0.125, where the interactions between the landslide and the offshore-propagating waves were slight, the models provided reasonable predictions of the phasing and amplitudes of the waves in the vicinity of the landslide. The model predictions of these waves worsened with increasing Froude number.

As discussed in Sect. 5, a free surface depression formed above the landslide during its constant-velocity motion. Both models under-predicted the amplitude of this depression at $Fr = 0.125$, although again the inclusion of the nonlinear bottom boundary condition lessened this under-prediction. At this Froude number, the models also slightly over-estimated the amplitude of the offshore-propagating trough (located at approximately $x = 2.5$) after it passed over the landslide. Some additional phase discrepancies are also evident close to the landslide. Hence, it appears that the models were unable to correctly predict the effect of the landslide on those waves passing above it. These effects became much more pronounced with increasing Froude number, with the models over-predicting the amplitudes of the waves in front of the landslide but significantly under-predicting the amplitudes of the waves above or behind the landslide. Although the nonlinear model did not exhibit the same amount of amplitude under-prediction as the linear model, both models failed to capture the phasing of the waves around the landslide at $Fr = 0.250$ and 0.375 . These incorrect predictions of the phasing, and overall behaviour, of the waves in the vicinity of the landslide appear to be relatively unaffected by the bottom boundary condition. The assumed linearity of the free surface boundary conditions is far more likely to account for these discrepancies, consistent with the applicability limits stated by Lee et al. [19].

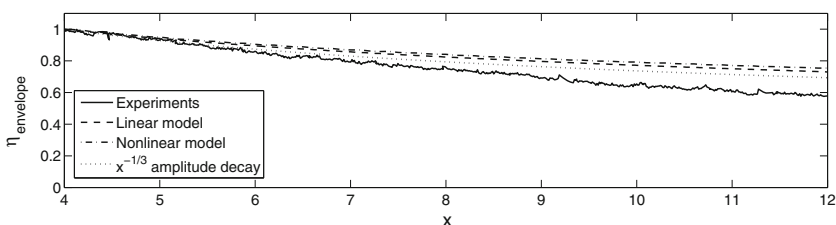


Fig. 13 Comparison of measured and predicted amplitude envelope decay in the positive x -direction

The models were also unable to correctly predict the amplitudes of the waves directly behind the free surface depression. The waves in this region were weakly nonlinear, and nonlinear steepening appeared to slightly reduce the effects of dispersion (i.e. the broadening of wave fronts and separation of different wavelengths) on these waves. Thus, the models predicted larger wave amplitudes in front of the landslide, but smaller amplitudes above and behind the landslide. This indicates the generation of the trailing waves predicted by Lee et al. [19], and a transition between an acceleration dominated regime to a Froude number dominated regime.

Figure 14 compares the model predictions of the potential energy within the wave field to the values calculated from the experimental measurements. The models captured the initial increase in energy during the acceleration phase, although they under-predicted the magnitude of the energy contained within the wave field during this phase of motion. This demonstrates that the models under-predicted the amplitudes of both leading waves during the landslide acceleration, leading to an under-prediction of the wave field potential energy. The models also under-predicted the peak potential energy at each Froude number, which occurred during the constant-velocity phase of motion. As with the generated wave amplitudes, the nonlinear model predictions were closer to the experimental values. This demonstrates that the nonlinear boundary condition was more effective in predicting the energy imparted by the landslide to the wave field. The models generally captured the time-dependent behaviour of the potential energy within the wave field, with the exception of the final stages of the constant-velocity phase of motion at $Fr = 0.375$. Despite being formulated according to linear wave theory, both models also predicted the directional mass transport observed in Fig. 9, with slight under-predictions of the magnitude of the mass transport.

In summary, the models performed well at predicting the amplitudes and phasing of the waves produced by a low-Froude number landslide. The nonlinear bottom boundary condition provided more robust predictions of the energy imparted by the landslide acceleration to the wave field, although both models still under-predicted the wave amplitudes in all of the experiments. As the Froude number increased, the model predictions became poor in the vicinity of the landslide. This is likely due to nonlinear effects on the waves in this region, since the models could only predict their frequency-dispersive behaviour.

6.4 Application to sloping-boundary experiments and field scenarios

The current experiments provide insights into the effect of submergence depth, landslide acceleration and terminal velocity on the properties of waves generated over a horizontal

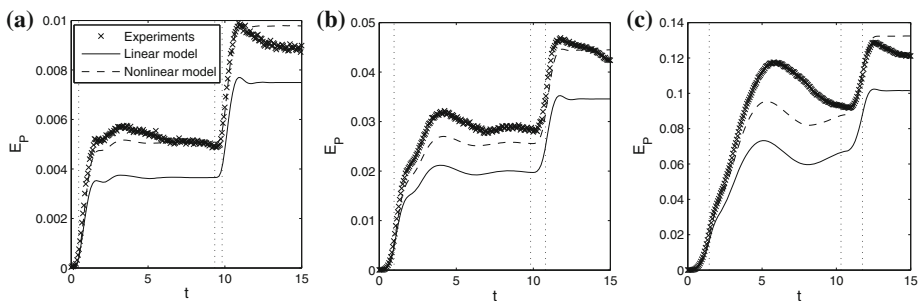


Fig. 14 Numerical model predictions of the potential energy within the wave field, for experiments with $\lambda = 0.153$, $\tau = 0.35$ and **a** $Fr = 0.125$, **b** $\tau = 0.250$, **c** $\tau = 0.375$

boundary. Before applying these findings to a field scenario, it is important to consider the differences between the waves generated by the motion of a solid block along a horizontal boundary and a sloping boundary. A landslide moving along a sloping boundary will begin its acceleration in the shallowest water depth. Thus, the waves generated by the landslide acceleration will have larger amplitudes than those generated during later phases of motion. Hence, the acceleration phase of landslide motion has the greatest influence on the properties of the generated waves in a sloping-boundary experiment [2, 35]. In the current experiments, the importance of the acceleration phase of motion depended on the landslide Froude number. As the Froude number increased, the constant-velocity phase of motion had a greater effect on the wave field behaviour. In previous experiments containing a sloping boundary, the landslide often did not achieve a sustained period of constant velocity [32]. Such a period of constant velocity would only be attained over a long slope length, and even on shallow slopes the deeper water during this phase of motion would reduce the amplitudes of any generated waves. Only the lower Froude number experiments in the current study should be compared to previous sloping-boundary studies, since these experiments were most influenced by the landslide acceleration.

Both the horizontal boundary and sloping boundary experimental configurations are idealisations of a field scenario. A landslide is a complex mixture of granular material and entrained fluid. Correctly modelling a landslide as a granular material in a laboratory study can lead to difficulties with scale effects, as discussed by Heller et al. in the context of a subaerial landslide [13]. Modelling a landslide as a solid block is likely to over-estimate the amplitudes of the generated waves [29]. The angle and length of the failure slope will dictate the kinematics of a landslide in the field, and so it is difficult to obtain representative values for the landslide acceleration or terminal velocity. Additionally, field landslides may not be wide enough to justify a two-dimensional approximation to the problem. Lateral dispersion will cause wave amplitudes to reduce more rapidly, and may also lead to variations in run-up as discussed by Sammarco and Renzi [30].

7 Conclusions

This study has provided insight into the mechanism of wave generation by a submarine landslide, and the effect of the low Froude number landslide motion on both onshore- and offshore-propagating waves. The Froude number was found to be the dominant parameter affecting the wave field behaviour. The use of a horizontal boundary enabled measurement of the amplitudes and energy of the onshore-propagating waves; these measurements were not available in previous sloping-boundary experiments. At low Froude numbers, the energy in the two wave groups was approximately equal, with the offshore-propagating waves becoming more prominent at higher Froude numbers. The onshore-propagating waves are likely to be of the most concern to coastal communities in the event of a field landslide.

The mechanical system used during these experiments was able to provide highly repeatable landslide motion over a range of accelerations and terminal velocities. The generated wave field was also highly repeatable, and LIF measurements from 37 locations were combined to create the wave field over the entire flume length. This measurement technique allowed identification of the free surface location to sub-pixel accuracy, generating a high-quality data set for the validation of numerical models.

The ability to control the landslide motion enabled the investigation of the effect of different phases of landslide motion on the generated waves. The acceleration of the landslide generated a leading offshore-propagating crest and onshore-propagating trough, both of which were followed by a dispersive packet of waves. At low Froude numbers, the wave field was dominated by these waves. In this case, the difference between the off-shore- and onshore-propagating wave amplitudes was negligible. Both the inviscid-irrotational models predicted the phasing of these waves correctly, despite slightly underpredicting the wave amplitudes. Since these Froude numbers are more representative of sloping-boundary scenarios, these models may also be applied to gentle sloping-boundary scenarios.

At higher landslide Froude numbers, the wave field behaviour was governed by the interactions between the moving landslide and the offshore-propagating waves. The models did not correctly predict the amplitudes or phasing of the waves in the vicinity of the landslide. These discrepancies are likely to have been caused by the linear free surface conditions used by the models. However, the success of the models in predicting the wave field behaviour away from the generation zone indicates the importance of dispersion in landslide-generated tsunami problems.

The landslide submergence depth affected the amplitudes and the wavelengths of the generated waves, but had a negligible effect on the overall wave field behaviour. The initial landslide acceleration affected the amplitude of the dispersive wave packets, and determined the position of the landslide (within the offshore-propagating wave packet) at the start of its constant-velocity motion.

In future experiments, the effects of a sloping boundary could be considered by inclining the current experimental setup by a small angle ($<10^\circ$). This would create an experimental geometry that more closely represented the continental slope, allowing consideration of the effect of varying water depth on the onshore- and offshore-propagating waves. Additional beach elements could be added to investigate the run-up and overtopping caused by the generated waves. The current study used a trapezoidal motion profile to investigate the behaviour of waves during a period of constant velocity, however different motion profiles could also be tested.

Acknowledgments The laboratory work in this project was conducted with the assistance of Ian Sheppard, Kevin Wines, Alan Stokes and Mike Weavers. The contributions of Sarah Delavan and Pedro Lee, as well as the comments of the two anonymous reviewers, are also appreciated.

References

1. Di Risio M, De Girolamo P, Bellotti G, Panizzo A, Aristodemo F, Molfetta MG, Petrillo AF (2009) Landslide-generated tsunamis runup at the coast of a conical island: New physical model experiments. *J Geophys Res* 114(C1), C01,009
2. Enet F, Grilli ST (2007) Experimental study of tsunami generation by three-dimensional rigid underwater landslides. *J Waterw Port Coast Ocean Eng* 133(6):442–454
3. Fritz HM, Hager WH, Minor HE (2003) Landslide generated impulse waves. *Exp Fluids* 35(6):505–519
4. Fritz HM, Hager WH, Minor HE (2003) Landslide generated impulse waves. 2. Hydrodynamic impact craters. *Exp Fluids* 35(6):520–532
5. Fritz HM, Hager WH, Minor HE (2004) Near field characteristics of landslide generated impulse waves. *J Waterw Port Coast Ocean Eng* 130(6):287–302
6. Fritz HM, Mohammed F, Yoo J (2009) Lituya Bay landslide impact generated mega-tsunami 50th anniversary. *Pure Appl Geophys* 166(1–2):153–153-175
7. Grilli ST, Bengtson A, Watts P, Imamura F (2001) Benchmark cases for tsunamis generated by underwater landslides. *Ocean Wave Meas Anal* 2001:1505–1514

8. Grilli ST, Vogelmann S, Watts P (2002) Development of a 3D numerical wave tank for modeling tsunami generation by underwater landslides. *Eng Anal Bound Elem* 26(4):301–313
9. Grilli ST, Watts P (1999) Modeling of waves generated by a moving submerged body. Applications to underwater landslides. *Eng Anal Bound Elem* 23(8):645–656
10. Grilli ST, Watts P (2005) Tsunami generation by submarine mass failure. I: modeling, experimental validation, and sensitivity analyses. *J Waterw Port Coast Ocean Eng* 131(6):283–297
11. Hampton MA, Lee HJ, Locat J (1996) Submarine landslides. *Rev Geophys* 34(1):33–59. doi:<http://dx.doi.org/10.1029/95RG03287>
12. Heinrich P (1992) Nonlinear water waves generated by submarine and aerial landslides. *J Waterw Port Coast Ocean Eng* 118(3):249–266
13. Heller V, Hager WH, Minor HE (2008) Scale effects in subaerial landslide generated impulse waves. *Exp Fluids* 44(5):691–703 doi:<http://dx.doi.org/10.1007/s00348-007-0427-7>
14. Imamura F, Hashi K (2003) Re-examination of the source mechanism of the 1998 Papua New Guinea earthquake and tsunami. *Pure Appl Geophys* 160(10):2071–2086
15. Jiang L, LeBlond PH (1992) The coupling of a submarine slide and the surface waves which it generates. *J Geophys Res* 97(C8):12731–12744
16. Jiang L, LeBlond PH (1993) Numerical modeling of an underwater Bingham plastic mudslide and the waves which it generates. *J Geophys Res* 98(C6):10303–10317
17. Jiang L, Leblond PH (1994) Three-dimensional modeling of tsunami generation due to a submarine mudslide. *J Phys Oceanogr* 24(3):559–572
18. Kaijura K (1963) The leading wave of a tsunami. *Bull Earthq Res Instit* 41(33):535–571
19. Lee SJ, Yates GT, Wu TY (1989) Experiments and analyses of upstream-advancing solitary waves generated by moving disturbances. *J Fluid Mech* 199:569–593
20. Lighthill J (1978) *Waves in fluids*. Cambridge University Press, Cambridge
21. Locat J, Lee HJ (2002) Submarine landslides: advances and challenges. *Can Geotech J* 39(1):193–212
22. Lynett PJ, Borrero JC, Liu PLF, Synolakis CE (2003) Field survey and numerical simulations: a review of the 1998 Papua New Guinea tsunami. *Pure Appl Geophys* 160(10):2119–2146
23. Matsumoto T, Tappin DR (2003) Possible coseismic large-scale landslide off the northern coast of Papua New Guinea in July 1998: geophysical and geological results from SOS cruises. *Pure Appl Geophys* 160(10):1923–1943
24. Mei CC, Stiassnie M, Yue DKP (2005) *Theory and applications of ocean surface waves: linear aspects*, vol. 23. World Scientific
25. Nokes R (2014) *Streams 2.02: system theory and design*. University of Canterbury
26. Pelinovsky E, Poplavsky A (1996) Simplified model of tsunami generation by submarine landslides. *Phys Chem Earth* 21(12), 13–17 doi:[http://dx.doi.org/10.1016/S0079-1946\(97\)00003-7](http://dx.doi.org/10.1016/S0079-1946(97)00003-7). Tsunamis Impacting on the European Coasts: Modelling, Observation and Warning
27. Qiu LC (2008) Two-dimensional SPH simulations of landslide-generated water waves. *J Hydraul Eng* 134(5):668–671
28. Renzi E, Sammarco P (2010) Landslide tsunamis propagating around a conical island. *J Fluid Mech* 650(1):251–285
29. Rządiewicz SA, Mariotti C, Heinrich P (1997) Numerical simulation of submarine landslides and their hydraulic effects. *J Waterw Port Coast Ocean Eng* 123(4):149–157
30. Sammarco P, Renzi E (2008) Landslide tsunamis propagating along a plane beach. *J Fluid Mech* 598(1):107–119
31. Satake K, Tanioka Y (2003) The July 1998 Papua New Guinea earthquake; mechanism and quantification of unusual tsunami generation. *Pure Appl Geophys* 160(10–11):2087–2118
32. Sue L, Nokes R, Davidson M (2011) Tsunami generation by submarine landslides: comparison of physical and numerical models. *Environ Fluid Mech* 11(2):133–165
33. Sue LP (2007) *Modelling of tsunami generated by submarine landslides*. Ph.D. thesis, University of Canterbury
34. Synolakis CE, Bardet JP, Borrero JC, Davies HL, Okal EA, Silver EA, Sweet S, Tappin DR (2002) The slump origin of the 1998 Papua New Guinea tsunami. *Proc Math Phys Eng Sci* 458(2020):763–789
35. Watts P (2000) Tsunami features of solid block underwater landslides. *J Waterw Port Coast Ocean Eng* 126(3):144–152
36. Weiss R, Fritz HM, Wannemann K (2009) Hybrid modeling of the mega-tsunami runup in Lituya Bay after half a century. *Geophys Res Lett* 36(9), L09,602
37. Whittaker CN (2013) *Modelling of tsunami generated by the motion of a rigid block along a horizontal boundary*. Ph.D. thesis, University of Canterbury